

New Prospects for High Performance SONAR, Chemical Sensor, and Communication Device Materials

Tingting Qi, Sergey V. Levchenko, Joseph W. Bennett, Ilya Grinberg, and Andrew M. Rappe
The Makineni Theoretical Laboratories, Department of Chemistry, University of Pennsylvania,
Philadelphia, PA
{tqi, slevchen, bennett4, ilya2, rappe}@sas.upenn.edu

Abstract

Perovskite oxides are a special group of materials, which exhibit many interesting properties, such as ferroelectricity, ferromagnetism, superconductivity, and high dielectric constant. Their unique physical properties lead to a variety of technological applications. Using quantum-mechanical simulations, we have computationally investigated several perovskite materials for use in Naval SONAR, chemical sensor and communications devices. We elucidate the influence of the constituent elements on technologically relevant properties, furthering the goal of achieving higher performance through modification of the material chemical composition.

1. Introduction

There is a growing demand for perovskite oxides (formula ABO_3) with better functionality and performance for use in many different types of applications, such as sensing, data storage, and energy conversion. In current military SONAR devices, perovskite solid solutions with high piezoelectric response are used. When such a material is deformed by the external underwater sound vibrations, it generates an electric field which can then be interpreted to gain information about depth, distance, and the identity of the source of the sound. Currently, intense efforts are underway to discover alterations in the chemical composition of the material that will enhance the piezoelectric constant and the operational temperature range. The direction of the ferroelectric material's spontaneous polarization can be reversed using an applied electric field. This is exploited extensively in high-density non-volatile random access memory (NVRAM) devices, currently based on the $Pb(Zr,Ti)O_3$ solid solution. Non-polar perovskites such as $BaZrO_3$ are used for their dielectric properties as capacitors in mobile

communication devices. Perovskites are also widely used in Solid Oxide Fuel Cells (SOFCs), such as the cathode material lanthanum strontium cobalt ferrite (LSCF).

The complexity of these multicomponent systems is crucial for their high technological performance. It also creates a large phase space for possible variation in compositions. Highly accurate modeling is necessary to understand the origin of the excellent properties exhibited by perovskites used in the current state-of-the-art technology and to speed up the design of new materials with enhanced performance for the devices of the future.

Over the last decade, first-principles calculations have emerged as vital tools for understanding complex solid state systems due to a combination of methodological improvements and faster computer speeds. In particular, density functional theory (DFT) is an extremely successful approach for the description of ground state properties of metals, semiconductors, and insulators^[1,2] due to a combination of accuracy and computational efficiency. Here, we report on our recent DFT studies of the highly tetragonal lead-free ferroelectric material $Bi(Zn_{1/2}Ti_{1/2})O_3$ $PbTiO_3$ ^[3], our prediction of the relative thermodynamic stability of ferroelectric (FE) lithium niobate ($LiNbO_3$) (0001) surfaces of different stoichiometry^[4] and on our investigation of the dielectric properties of the $Ba_{1-x}Ca_xZrO_3$ materials promising for use in communication devices^[5].

2. Methodology

Our calculations are performed with both our in-house code BH (used in previous studies^[6,7]) and the ABINIT software package using either the standard LDA^[8] or GGA^[9] exchange-correlation functional. We use a plane-wave basis set, which is a complete basis set that offers the advantage of carrying out operations in both real and reciprocal space through fast Fourier transforms. To reduce the computational cost of the calculations, we use designed non-local^[10] optimized^[11]

pseudopotentials to represent the interactions of the nucleus and the core electrons with the valence electrons. Minimization of the energy with respect to the electronic degrees of freedom is done using the blocked-Davidson^[12] iterative diagonalization procedure^[13] with Pulay density mixing^[14]. Ionic minimization is performed using a quasi-Newton algorithm^[15]. DFT calculations are performed on supercells of up to 60 atoms, with a variety of atomic configurations examined to ensure accurate modeling of the disordered perovskite structures.

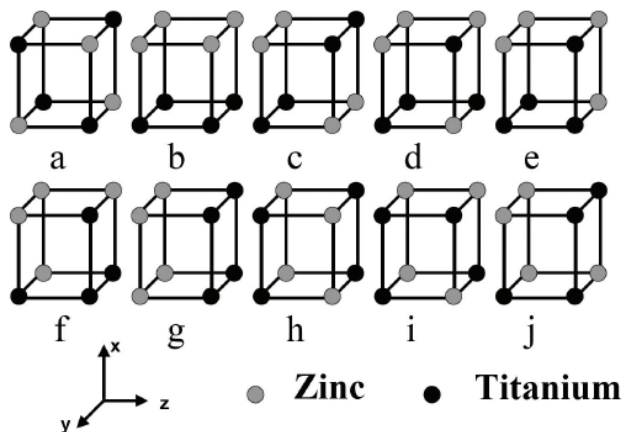


Figure 1. Ten B-cation arrangements for 40-atom tetragonal BZT supercells^[3]

3. Results

3.1. First-Principles Investigation of a Highly Tetragonal Ferroelectric Material: $\text{Bi}(\text{Zn}_{1/2}\text{Ti}_{1/2})\text{O}_3$ (BZT)

The $\text{PbZr}_{1-x}\text{Ti}_x\text{O}_3$ (PZT) solid solution at the morphotropic phase boundary composition is the most widely used piezoelectric material today. Solid solutions with higher Curie temperature that enables a broader temperature range of operation are currently under active research. First-principles calculations were performed to study the extremely tetragonal ferroelectric material BZT using all possible Zn/Ti arrangements in a $2 \times 2 \times 2$ 40-atom supercell. These supercell arrangements are shown in Figure 1. In agreement with experiment^[16], we find that BZT displays extremely large cation displacements and tetragonality. Despite its high tetragonality and polarization, the local structure of the material exhibits a high degree of disorder, which is more typical of the solid solutions close to the morphotropic phase boundary.

We find that the cation displacements and strain are extremely large in BZT. All supercells, except supercell c, are highly polar with P values in the 1.35–1.43 C/m^2 range. Such a large polarization is enabled by the

extreme tetragonality of the material with c/a values in the 1.27–1.29 range. Our calculated polarization values are higher than the estimate obtained by Suchomel et al.^[16] (1.03 C/m^2). We believe that the previous estimate is too low, due to the use of formal charges to calculate P . These are smaller than the Born effective charges (Z^*) that must be used for calculating polarization. The 1.38 C/m^2 average polarization found for BZT is to our knowledge the largest known polarization for a stable ground state of a material. To estimate the ferroelectric to paraelectric transition temperature T_c , we use the calculated polarization value in conjunction with the previously established^[17] relationship between P and T_c in Bi-containing ferroelectric solid solutions. Using the proportionality constant between T_c and P^2 obtained from previous work (870 $\text{K}\text{m}^4/\text{C}^2$)^[17], we estimate T_c of BZT as 1,656K. This is higher than the highest known perovskite T_c of 1,400K obtained for LiNbO_3 .

We find that the energetics of the B-cation arrangement for the rhombohedral and the tetragonal phases of BZT are significantly different. For the rhombohedral phase, the lowest energy B-cation arrangement is the rocksalt ordering of Zn and Ti. This is in agreement with the expectations of the standard electrostatic model for B-cation arrangement in perovskites. The correct energy ranking can be obtained even without taking the cation displacements into account, as can be shown by a comparison of the electrostatic energy differences for undistorted BZT structures and the relaxed rhombohedral phase structure (Figure 2). Comparison of our data to the literature studies^[18] of B-cation ordering in the $\text{Pb}(\text{Sc}_{1/2}\text{Nb}_{1/2})\text{O}_3$ (PSN) material shows that the energy difference between the electrostatically favored (111) B-cation ordering and the less favored (100) ordering is four times smaller in BZT than in PSN. This is due to the higher covalency and the larger off-center displacements of Bi cations relative to the Pb cations. In PSN, the Pb $6s$ –O $2p$ hybridization enables bonding of Pb cations to the underbonded oxygen atoms, reducing the energy cost of deviation from the (111) B-cation arrangement^[18]. Bi exhibits even greater covalency and hybridization than Pb, enabling Bi displacement to better compensate for underbonding of the oxygen atoms by their B-site neighbors. Thus, in the rhombohedral phase, the cation distortions set the scale of the energy differences between the different B-cation orderings, while the electrostatics determines the energy ranking.

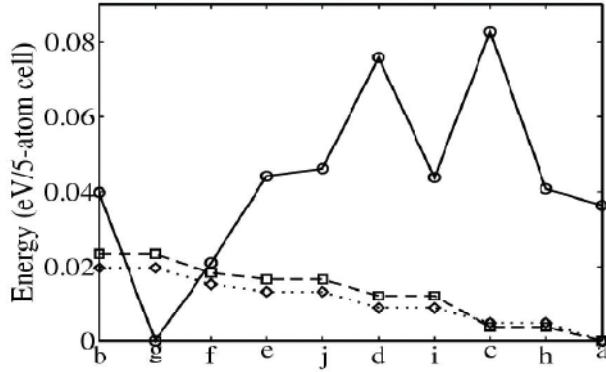


Figure 2. DFT energy differences from the lowest energy B-cation arrangement shown for the relaxed tetragonal (circles, solid line) and rhombohedral (squares, dashed line) structures. Also shown are the electrostatic energy differences for the relaxed cubic structures computed using formal ionic charges (diamonds, dotted line). To facilitate comparison, the energy differences for the cubic structures are scaled down by a factor of 100.^[3]

Surprisingly, for the tetragonal phase of BZT, the lowest energy B-cation arrangement is planar ordered (001) Zn/Ti stacking with the stacking direction perpendicular to the polarization direction. This preference is highly unusual and has been found only for the $\text{La}(\text{Cu},\text{Sn})\text{O}_3$ perovskite. We believe that it is the extreme tetragonality of BZT that changes the B-cation arrangement preference from (111) to (001).

The unusual preference of BZT for a (001) B-cation ordering suggest that interactions other than electrostatics make important contributions to the energetics of B-cation ordering in extremely tetragonal materials. We focus our investigation on the repulsive interaction between the A-site and B-site cations. This arises due to unfavorable wavefunction overlap between the A- and B-atom wavefunctions and has been found to be important for compositional phase transitions in ferroelectrics^[19,20]. The repulsion between A-site and B-site cations is particularly strong for materials where the large A-site displacements from high symmetry decrease the A-B-cation distances, as in the case of BZT. Previous research has found that the A-B repulsions are stronger for the cations with higher charge. We, therefore, expect the Bi-Ti repulsion to be more important than the Bi-Zn repulsion. To measure the strength of repulsion, we use the position of the first peak in the Bi-B-cation partial pair-distribution function (PDF).

To increase the Bi-Ti distance and to decrease the Bi-Ti wavefunction overlap, Bi cations favor displacing toward Zn. Such a preference can be best satisfied by the B-cation arrangements where Zn and Ti cations are grouped separately. In contrast, electrostatic interactions favor maximum dispersal of Zn and Ti. For the (001) planar ordering of Zn and Ti, this preference is easily satisfied and gives rise to a Bi-Ti peak at 3.48 Å and a

low repulsive energy. Similarly, longer Bi-Ti distances and low repulsion are found in supercell f due to the clustering of Zn and Ti cations.

For the rocksalt structure of supercell a, the full mixing of Zn and Ti atoms makes it impossible for Bi displacements to avoid the Ti atoms, leading to a Bi-Ti peak at 3.28 Å and a high repulsive energy. For the (100) planar Zn and Ti ordering found in supercell b, the large Bi displacements along (100) that are required by the strain-polarization coupling make Bi-Ti distances shorter than in (001) structure and raises the energy of supercell b. Thus, the high c/a ratios found in BZT increase the importance of the cation-cation repulsions and give rise to the anomalous B-cation ordering energetics found in BZT.

3.2. The Influence of Ferroelectric Polarization on the Equilibrium Stoichiometry of Lithium Niobate (0001) Surfaces

Stabilization mechanisms of polar oxide surfaces are currently under investigation due to their importance for understanding oxide functional properties in both natural and technological processes^[21,22]. Even without electrodes, charged surfaces can lower their energy in a variety of ways, such as surface metallization, reconstruction, molecular adsorption, or through changes in the surface stoichiometry^[23–29]. The stoichiometry and oxidation state of the atoms at the surface depends on the particular stabilization mechanism; this, therefore, plays a crucial role in determining the surface chemistry characteristics such as preferred adsorption sites, energetics, and atom exchange between the surface and the reactants and products in surface chemical reactions.

Here, we report on our theoretical study of ferroelectric LiNbO_3 (LN) (0001) surfaces. This system is of both fundamental and practical interest. LN has a single stable crystal phase, with ferroelectric polarization directed along (0001), that is also an intrinsically polar direction. Due to these properties, LN has attracted attention as a heterogeneous catalyst^[30–34]. We use *ab initio* thermodynamics approach to calculate the relative stability of LN surfaces of different stoichiometry for positive and negative bulk polarization under a range of temperatures and oxygen pressures.

We find that the structure and composition of positive and negative surfaces under the same experimental conditions is quite different. The most stable LN surface terminations under different ambient conditions in the absence of foreign adsorbates are shown in Figure 3. Space-fill models of some of the stable surface terminations are presented in Figure 4.

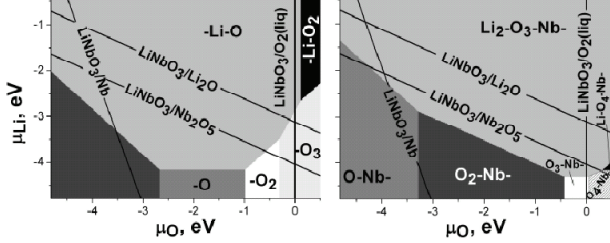


Figure 3. Stable surface terminations of negative (left) and positive (right) surfaces of LN. The terminations are labeled with hyphens. The unlabeled region corresponds to an Nb-terminated surface. The black lines denote boundaries beyond which new bulk phases (shown on corresponding lines) start to precipitate on the LN surfaces. The region where only bulk LN phase is stable is within the trapezoid formed by the black lines.^[4]

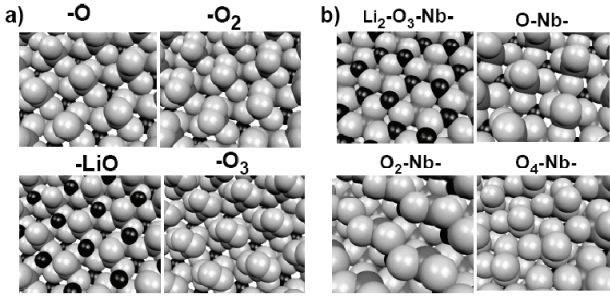


Figure 4. Space-fill models of LN negative (a) and positive (b) surface terminations stable at various conditions. Li is black, Nb is gray, and O is light gray.^[4]

The -Li-O termination is favored under most conditions (Figure 3, left), if the spontaneous bulk polarization vector is directed away from the surface (negative surface). If the spontaneous bulk polarization vector is directed toward the surface (positive surface), the surface will contain more oxygen than the negative surface at similar conditions (Figure 3, right). Under chemical potential conditions where bulk LN is stable, the $\text{Li}_2\text{-O}_3\text{-Nb-}$ termination (i.e., one extra Li atom per surface cell above stoichiometric tri-layers) has the lowest free energy for all conditions. An interesting feature of the $\text{Li}_2\text{-O}_3\text{-Nb-}$ termination is that one Li relaxes down into the top oxygen plane, while the other Li stays above the oxygen plane.

Our calculations suggest that the surface loses $2(\text{LiO})$ and becomes terminated by O-Nb- under low μ_{O} conditions. It is interesting to note that the positive surface prefers to lose two Li atoms at low μ_{Li} instead of losing them one by one.

The stability of the preferred terminations of positive and negative surfaces of LN can be explained by the need to passivate the surface charge generated by the bulk polarization. To model the passivation, we develop an ionic model based on the formal oxidation states $q_{\text{Nb}}=+5e$, $q_{\text{O}}=-2e$, $q_{\text{Li}}=+e$, to calculate the surface charges of stoichiometric paraelectric-like LN slab with equally-

spaced LiO_3 and Nb layers, terminated with a LiO_3 layer on one side, and a Nb layer on the other side. Here, the stoichiometric PE-like slab would have surface charges of $-5e/2$ per surface unit cell on the LiO_3 -termination and $+5e/2$ on the -Nb termination. This creates a potential difference of $\Delta\phi \approx 20$ VÅ. To avoid the potential difference, the charges must be passivated by either mobile charges (electron transfer), or stoichiometry changes (adding charged ions) or some combination of the two. Our results demonstrate that passivation by ions is thermodynamically favored over the passivation by the mobile charges.

Among stoichiometric PE-like phases (holding all layers fixed with O and Li coplanar), we find that transfers of O (ionic charge of $-2e$) or O_2Li ($-3e$) from the LiO_3 surface to the Nb surface are the most stable, lowering the energy by 4.6 eV/cell (converged with respect to the slab thickness). Within a 1×1 surface cell, these two choices optimally reduce the model surface charges, from $\mp 5e/2$ per surface cell to $\mp e/2$ with O transfer or to $\mp e/2$ with O_2Li transfer. Thus, in the case of paraelectric LN, passivation with ions is more favorable than passivation with mobile charges.

We now extend this model to ferroelectric LN. The polarization of the PE LN is non-zero, because of the polar stacking of ionic layers, whose net charge per unit cell is odd. For $P_{\text{PE}} \neq 0$, the ferroelectric contribution to the total polarization is $P_{\text{tot}} - P_{\text{PE}}$, computed with the same layer stacking within the unit cell for FE and PE. To compute the polarization values, we use the Berry's phase approach^[35]. This allows calculations of polarization for a non-magnetic insulator within an even integer multiple $2N$ of a polarization quantum. In the case of LN, the polarization quantum per hexagonal unit cell is $eR/\Omega = e/S$, where R is the length of the lattice vector along the (0001) direction, Ω is the volume of the unit cell, and S is the area of the surface unit cell. We find $P_{\text{tot}} - P_{\text{PE}} = (2N \times 0.69 + 0.86) \text{ C/m}^2 \approx (2N + 5/4)e/S$. Analysis of the changes in polarization represented as a product of Born effective charges and atomic displacements finds that the polarization change going from PE to FE is correct for $N=0$. Thus, the presence of FE displacements adds surface charge of $5e/4$ per surface cell to the stoichiometric Li-O_3 (0001) surface and $-5e/4$ to the Nb-terminated surface, leaving the Li-O_3 -termination with net bound surface charge of $-5e/4$ and the -Nb termination with $+5e/4$ in the FE phase.

Our analysis of polarization and surface charge explains the observed stable surface stoichiometries on the FE surfaces of LN. For the stoichiometric $\text{Li-O}_3\text{-Nb-}$ (0001) surface, the net bound charge is $-5e/4$. Addition of an extra Li atom (surface denoted $\text{Li}_2\text{-O}_3\text{-Nb-}$) stabilizes a hole and, within the simple ionic model, reduces the charge to $-e/4$ in the insulating state. On the

bottom surface, the Nb termination has bound charge of $+5e/4$, and addition of $-O-Li$ stabilizes charge of $-e$ reducing the net surface charge to $+e/4$. The remaining $\pm e/4$ can be passivated with mobile charges or with sub-monolayer coverage of additional ions, depending on the ambient conditions and sample history. Thus, our first-principles thermodynamic modeling demonstrates that ionic passivation of the surface charge is favored. The surface charge is given by a simple ionic model taking into account both ferroelectric polarization and intrinsic polar stacking.

3.3. Non-Monotonic Composition Dependence of the Dielectric Response of $Ba_{1-x}Ca_xZrO_3$ (BCZ)

Dielectric materials used in wireless communication applications require a high dielectric constant, ϵ , and a low dielectric loss^[36]. Many of the current devices are based on the perovskite barium zirconate, $BaZrO_3$ (BZ) and its solid solutions. Experimentally, it was shown that the dielectric constant of BZ can be increased by up to 50% by doping with small amount of Ca^[37] as seen in Figure 5. This effect is counterintuitive because $CaZrO_3$ (CZ) has a lower ϵ than BZ. Similar nonmonotonic dependence of ϵ on composition was observed in Ba-based perovskites with other B-site compositions^[38-41]. To understand the effects of Ca doping into BZ, we studied the BCZ solid solution at a variety of compositions^[37]. Our calculations reveal a new vibrational mechanism that arises due to the changes in the local structure of the perovskite A-site and leads to an enhanced dielectric response.

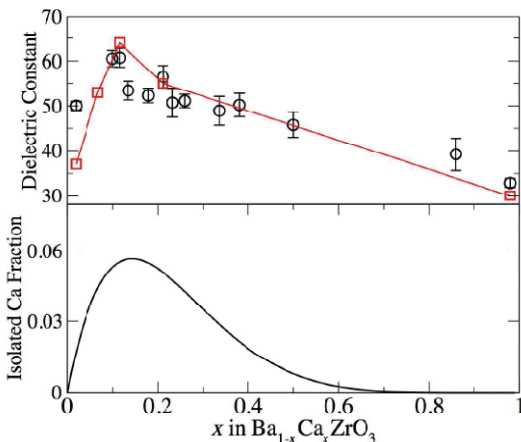


Figure 5. The directionally averaged ($T=0$ K) dielectric constant ϵ vs. Ca content x in BCZ. The ϵ values are also averaged over cation orderings. Black circles are the averaged diagonal elements of the ϵ tensor. Low T experimental values^[37] are shown as red squares. Also shown is the fraction of isolated Ca atoms, $x(1-x)^6$, as a function of x .^[5]

The A-site local structure undergoes significant changes due to the introduction of Ca atoms into BZ. In BZ, the Ba atoms are located at the high-symmetry positions in the center of the O_{12} cage. In contrast, due to their smaller ionic size Ca atoms in BCZ off-center along the (100) direction toward a low-symmetry position to satisfy bonding requirements. Ca displacements increase with increased Ca content, from 0.3 Å at $x=0.125$ to Å at 0.5 Å at $x=0.5$.

In agreement with experimental data, we find that at low Ca content, the dielectric constant of BCZ ($\epsilon=65$) is greater than that of BZ ($\epsilon=50$). Comparison of BCZ and BZ phonon modes shows that the breaking of symmetry induced by $x=0.125$ Ca doping broadens the discrete Γ point phonon frequencies of BZ (Figure 6(a)). Ca doping also introduces IR-active phonon modes at frequencies that are not present in BZ. In the parent $BaZrO_3$ material, three sets of IR-active modes contribute to ϵ . The lowest-frequency phonon modes occur around 110 cm^{-1} and make the largest contribution to the dielectric constant. These phonons are due to Ba rattling inside its O_{12} cage. In $CaZrO_3$, the A-site driven phonons (known as the Last type phonon modes) exhibit vibrational frequencies of 96, 106, and 191 cm^{-1} . In BCZ, at low x , the introduction of Ca leads to appearance of A-site driven vibrational phonons at 40 cm^{-1} , 49 cm^{-1} , and 60 cm^{-1} , lower than the Last mode frequencies in either BZ or CZ. The presence of such low frequency modes significantly enhances the dielectric constant, as ϵ is proportional to $1/\omega^2$.

The new low-frequency vibrations are localized around the Ca site and consist of mainly Ca-O vibrations into which some Ba-O motion is mixed. This is unlike the delocalized last type phonon modes in both BZ and CZ, which extend throughout the whole material. However, the Ca vibration in its O_{12} cage in low-frequency modes of BCZ is similar to that found in CZ. For $x=0.125$ composition, Ca off-centers along the (001) axis. This forms a stronger Ca-O bond in the direction of displacement and elongates Ca-O bonds in the other two Cartesian directions. The weakened bonds lead to a low frequency of Ca oscillations perpendicular to the Ca displacement, giving rise to two low frequency modes at 45 cm^{-1} and 49 cm^{-1} . Ca oscillation in the direction of Ca off-center displacement has a higher mode frequency (60 cm^{-1}), suggesting a stronger bond. The Ca-O modes in the CZ are located at significantly higher frequencies (96 cm^{-1} , 106 cm^{-1} , and 191 cm^{-1}). The lower frequencies of Ca-O oscillations in BCZ are due to the large volume of the $Ca-O_{12}$ cage stretching the Ca-O bonds. Bond-valence sums support our DFT finding of weaker Ca-O bonds in BCZ. We find that Ca bond valence computed using relaxed DFT structures is 1.8 for Ca in BCZ and 2.05 for Ca in CZ. Similar conclusions about the weak bonding

for Ca in BCZ were reached by Levin et al. using bond valence analysis of structures obtained from refinement of neutron diffraction data^[37].

Analysis of the local structure and phonon modes provides a clear picture of the mechanism for the compositional dependence of the dielectric constant in BCZ. As Ca content increases, the A-O and B-O BZ-derived modes are further broadened over a wider range of frequencies (Figures 6(a) and 6(b)). The total directionally averaged B-O contribution to the dielectric constant is around 20, and the O_6 and electronic contributions are both ≈ 5 for all compositions. The Ca-O rolling cation modes undergo the largest changes, as an increase in Ca content gives rise to stronger Ca-O bonds in all three Cartesian directions and an increase in the phonon frequencies for the rolling cation modes. Despite the stronger intensity of the low-frequency Ca-O modes at $x=0.25$, their contribution to the dielectric constant decreases relative to $x=0.125$ due to the blueshift in the Ca-O mode frequencies and the $1/\omega^2$ dependence of the dielectric constant. Therefore, the overall BCZ ϵ decreases from $x=0.125$ to $x=0.25$. As x is increased past 0.25, there is a further upshift of the Ca-O modes due to stronger Ca-Ca interactions. For $x>0.5$, we find a general shift to higher ω values, further decreasing the dielectric response.

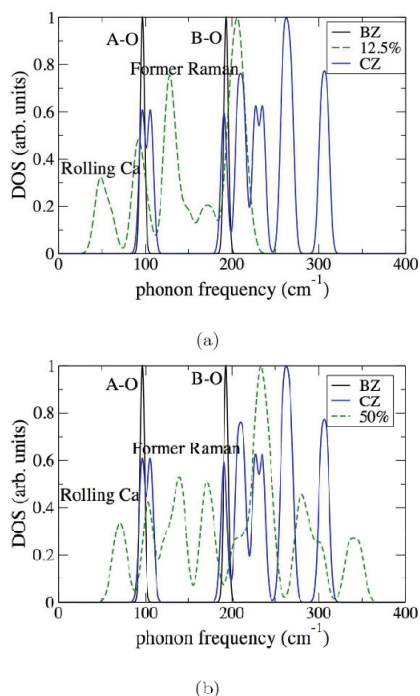


Figure 6. IR active phonon frequency comparisons of $2\times 2\times 2$ BCZ to BZ, shown in black, and CZ, shown in blue. Not shown are O_6 modes above 400 cm^{-1} , which do not shift as significantly. a) $\text{Ba}_{0.875}\text{Ca}_{0.125}\text{ZrO}_3$. b) $\text{Ba}_{0.50}\text{Ca}_{0.50}\text{ZrO}_3$. All show IR active low frequency phonon modes that are not present in either BZ or CZ, as well as more modes centered around 130 cm^{-1} .^[5]

The non-monotonic dielectric constant dependence on composition can be traced directly to the changes in the local structure with increasing Ca content. At small x , due to the localized nature, of the low frequency modes the Ca-Ca interactions do not affect the Ca-O vibrational frequencies. Therefore, an increase in Ca concentration leads to a linear increase in the intensity of the low-frequency Ca modes and ϵ .

The *decrease* of the dielectric constant with increasing Ca content is due to the effect of Ca atoms in close proximity to one another, which occurs frequently for non-dilute solid solution compositions. A Ca atom fully surrounded by Ba neighbors displaces along (100). When two Ca atoms are found next to each other in a 40-atom supercell ($x = 0.25$), their displacements are still mostly in (100), but components along the other Cartesian directions are present also. This is because the close proximity of the small Ca cations induces large O_6 tilts and limits the available volume for displacements. This effect becomes more pronounced with higher Ca content, until large displacements along (100) are no longer possible and smaller displacements are made along (111). Since the off-center displacements along the (101), (101) and (011) directions strengthen the Ca-O bonds, the rotation of Ca displacement direction from (100) to (111) with increasing Ca content makes the Ca-O bonds at higher x more stiff, increasing the Ca-O vibrational modes' frequencies. This decreases ϵ .

The mechanism, by which the local structure affects the dielectric constant, described above implies that the ϵ should peak at compositions for which Ca-Ca interactions are weak. This suggests the peak ϵ will be located at x with the maximum population of Ca atoms fully surrounded by Ba atoms. Simple statistics show that in BCZ, this occurs at $x=0.14$, as shown in Figure 5. At this x , 6% of the A-sites in the material are occupied by the Ca atoms with only Ba nearest neighbors. This explains why the turnover in ϵ of BCZ takes place at low x , as observed experimentally and in our calculations. At low Ca concentrations, Ca-Ca interactions are rare and do not hinder the 'rolling cation' motion. As x increases, nearest Ca-Ca neighbors become frequent, decreasing the 'rolling cation' motion. This mechanism is due to a size mismatch on the perovskite A-site between the large majority cations and the small minority cations and does not depend on the particular chemistry of the A-site and B-site ions present in BCZ. Therefore, we expect this effect to be present for any case of doping of a perovskite with a large cation on the perovskite A-site with a smaller cation.

4. Significance to DoD

Perovskite oxides are used extensively in modern Naval SONAR devices, non-volatile memories and telecommunications applications. The US Navy would reap a considerable military advantage from developing SONAR-detecting materials and communication device materials with higher performance, lower cost and less harmful environmental side effects. Understanding the behavior of current perovskite oxides is critical for the goal of developing new materials. Once the relationships between the atomic composition, structure and materials properties are understood, new materials that improve upon existing technology can be designed. Our DFT calculations have revealed the microscopic origin of highly polarized material BZT, that can be used as a component in high-temperature piezoelectrics and elucidated the relationship between its composition and macroscopic properties. We have also obtained a understanding of the ferroelectric surface stabilization mechanism. A change in surface stoichiometry alters preferred adsorption sites, energetics, and atom exchange between the surface and the reactants and products in surface chemical reactions. It has been suggested that adsorption of different molecules, raising the possibility of creating ferroelectric chemical sensors. Also, we have studied the dielectric material BCZ, whose non-monotonic dielectric response has led us to propose a general mechanism that could lead to improved wireless communication applications.

Systems Used

The work presented here was performed on the Engineer Research and Development Center's Cray XT3 and XT4, the Arctic Region Supercomputer Center's Sun Opteron Cluster. With regards to our in-house code, ionic relaxations typically run in about a week on the XT3 and Opteron machines. DFT codes use an iterative diagonalization procedure to solve quantum mechanical calculations that rely heavily on BLAS and LAPACK routines. Typically, runs use 4 to 32 processors. This code is highly scalable with a parallelization efficiency of almost 100% for a small numbers of processors (<20) and dropping off to slightly above 50% at 128 processors.

Computational Technology Area

Computational Material Science

Acknowledgments

This work was supported by the Office of Naval Research under grant number N00014-00-1-0372, by the Department of Energy, Office of Basic Energy Sciences, under Grant No. DE-FG02-07ER15920, and by the NSF through the MRSEC grant, DMR05-20020. Computational support was provided by a Challenge grant from the HPCMP of the US Department of Defense.

References

1. Hohenberg, P. and W. Kohn, *Phys. Rev.*, 136, B864, 1964.
2. Kohn, W. and L.J. Sham, *Phys. Rev.*, 140, A1133, 1965.
3. Qi, T., I. Grinberg, and A.M. Rappe, *Phys. Rev. B*, 79, 094114, 2009.
4. Levchenko, S.V. and A.M. Rappe, *Phys. Rev. Lett.*, 100, 256101, 2008.
5. Bennett, J.W., I. Grinberg, and A.M. Rappe, *Chem. Mat.*, 20, 5134, 2008.
6. Mason, S.E., I. Grinberg, and A.M. Rappe, *Phys. Rev. B Rapid Comm.*, 69, 161401(R), 2004.
7. Bennett, J.W., I. Grinberg, and A.M. Rappe, *J. Amer. Chem. Soc.*, 130, 17409, 2008.
8. Perdew, J.P. and A. Zunger, *Phys. Rev. B*, 23, 5048, 1981.
9. Perdew, J.P., K. Burke, and M. Ernzerhof, *Phys. Rev. Lett.*, 77, 3865, 1996.
10. Ramer, N.J. and A.M. Rappe, *Phys. Rev. B*, 59, 12471, 1999.
11. Rappe, A.M., K.M. Rabe, E. Kaxiras, and J.D. Joannopoulos, *Phys. Rev. B Rapid Comm.*, 41, 1227, 1990.
12. Davidson, E.R., *J. Comput. Phys.*, 17, 87, 1975.
13. Bendtsen, C., O.H. Nielsen, and L.B. Hansen, *Appl. Num. Math.*, 37, 189, 2001.
14. Pulay, P., *J. Comp. Chem.*, 3, 556, 1982.
15. Pfrommer, B.G., M. Coté, S.G. Louie, and M.L. Cohen, *J. Comp. Phys.*, 131, 233, 1997.
16. Suchomel, M.R., A.M. Fogg, M. Allix, H. Niu, J.B. Claridge, and M.J. Rosseinsky, *Chem. Matter.*, 18, 4987, 2006.
17. Grinberg I. and A.M. Rappe, *Phys. Rev. Lett.*, 98, 037603, 2007.
18. Burton, B.P. and E. Cockayne, *Phys. Rev. B Rapid Comm.*, 60, 12542, 1999.
19. Grinberg I., V.R. Cooper, and A.M. Rappe, *Nature*, 419, 909, 2002.
20. Grinberg I., M.R. Suchomel, P.K. Davies, and A.M. Rappe, *J. Appl. Phys.*, 98, 094111, 2005.
21. Casey, W.H. and C. Ludwig, *Nature*, 381, 506, 1996.
22. Jupille, J., *Surf. Rev. Lett.*, 8, 69, 2001.
23. Noguera, C., *J. Phys. Condens. Matter*, 12, R367, 2000.
24. Finocchi, F., A. Barbier, J. Jupille, and C. Noguera, *Phys. Rev. Lett.*, 92, 136101, 2004.

25. Subramanian, A., L.D. Marks, O. Warschkow, and D.E. Ellis, *Phys. Rev. Lett.*, 92, 026101, 2004.
26. Staemmler, V., K. Fink, B. Meyer, D. Marx, M. Kunat, S.G. Girol, U. Burghaus, and Ch. Wöll, *Phys. Rev. Lett.*, 90, 106102, 2003.
27. Dulub, O., U. Diebold, and G. Kresse, *Phys. Rev. Lett.*, 90, 016102, 2003.
28. Ruberto, C., Y. Yourdshahyan, and B.I. Lundqvist, *Phys. Rev. Lett.*, 88, 226101, 2002.
29. Meyer, B., *Phys. Rev. B*, 69, 045416, 2004.
30. Choso, T., M. Kamada, and K. Tabata, *Appl. Surf. Sci.*, 121/122, 387, 1997.
31. Tabata, K., M. Kamada, T. Choso, and Y. Nagasawa, *J. Chem. Soc. Faraday Trans.*, 94, 2213, 1998.
32. Tabata, K., M. Kamada, T. Choso, and H. Munakata, *Appl. Surf. Sci.*, 125, 93, 1998.
33. Li, Z., T. Yu, and Z. Zou, *Appl. Phys. Lett.*, 88, 071917, 2006.
34. Yun, Y. and E. I. Altman, *J. Am. Chem. Soc.*, 129, 15684, 2007.
35. Vanderbilt, D. and R.D. King-Smith, *Phys. Rev. B*, 48, 4442, 1993.
36. Fortin, W., G.E. Kugel, J. Grigas, and A. Kania, *J. Appl. Phys.*, 79, 4273, 1996.
37. Levin, I., T.G. Amos, S.M. Bell, L. Farber, T.A. Vanderah, R.S. Roth, and B.H. Toby, *J. Solid State Chem.*, 175, 170, 2003.
38. Ikawa, H., M. Touma, T. Shirakimi, and O. Fukunaga, in *Electroceramics IV*, edited by R. Waser, S. Hoffman, D. Bonnenberg, and C. Hoffman, Verlag der Augustinus Buchhandlung, Achen, pp. 41–6, 1994.
39. Ikawa, H., M. Yashamiro, T. Niwa, T. Omata, and M. Takemoto, in *Electroceramics V*, edited by J.L. Baptista, L.A. Labrincha, and P.M. Vilarinho, University of Aveiro, Aveiro, pp. 41–4, 1996.
40. Ikawa, H. and M. Takemoto, *Mat. Chem. and Phys.*, 79, 222, 2003.
41. Ikawa, H., M. Takemoto, M. Katouno, and M. Takamura, *J. Eur. Ceram. Soc.*, 23, 2511, 2003.